Journal of Materials Chemistry B

ROYAL SOCIETY OF CHEMISTRY

PAPER

View Article Online
View Journal | View Issue

Cite this: J. Mater. Chem. B, 2025, 13, 7753

Suppression of the HSP90-HIF1α pathway with SNX2112-encapsulated nano-micelles for effective triple-negative breast cancer photothermal combined photodynamic therapy†

Zhiqi Zhang,‡[a] Fangzheng Tian,‡[a] Shiwei Lai,‡[a] Xiaoxuan Xu,[a] Mei Zhou,[a] Zhenyu Hou,[a] Siyu Li,[a] Jianqiong Zhang,[ab] Xue Yang,[a] Jinbing Xie*[a] and Shenghong Ju*[a]

Received 10th January 2025,
Accepted 19th May 2025

DOI: 10.1039/d5tb00071h

rsc.li/materials-b

Combined photothermal and photodynamic therapy is a promising strategy for the treatment of triple-negative breast cancer (TNBC) as it can accurately target tumor tissues and improve therapeutic efficacy. However, its efficacy is still insufficient owing to the heat resistance resulting from the upregulation of heat shock protein 90 (HSP90) and diminished reactive oxygen species (ROS) levels due to the accumulation of its client protein hypoxia-inducible factor-1α (HIF1α). Herein, SNX2112 (HSP90 inhibitor) and IR825 (photosensitizer) are loaded into a pH-responsive nano-micelle for efficient photothermal and photodynamic therapy. SNX2112 inhibits HSP90 activity to reduce heat resistance for enhanced photothermal therapy. Furthermore, HIF1α accumulation is reduced to increase ROS production to amplify photodynamic therapy efficacy. Consequently, the combined therapy enhanced by inhibiting HSP90-HIF1α effectively suppresses tumor growth *via* synergistic effects, with high photothermal conversion and ROS productivity under mild temperature (42 °C). Furthermore, using SNX2112 improves the efficacy of the combined photothermal and photodynamic therapy, showing its eminent potential in TNBC treatment.

1. Introduction

Clinically, surgery, chemotherapy and radiotherapy are cornerstones in triple-negative breast cancer treatment (TNBC).[1–3] However, they suffer from significant limitations, such as multidrug resistance of tumors or are highly cytotoxic to tumor and normal tissue cells with poor tumor targeting.[4,5] Photothermal therapy (PTT) and photodynamic therapy (PDT), achieved by elevating the temperature and generating reactive oxygen species (ROS), respectively, can ablate primary tumors with temporal and spatial selectivity, with fewer toxic and side effects.[6–9] While the complete eradication of solid tumors is difficult with PTT or PDT alone, the combination of PTT and PDT may offer the opportunity to utilize the benefits of each treatment modality to produce additional or even synergistic therapeutic effects. Studies have shown that the combination of photothermal and photodynamic therapies is promising for the treatment of tumors, including TNBC models.[10–12] ROS generated by PDT increases the oxidative stress in tumor cells and can be used as a trigger to promote the release of photosensitizers, thus enhancing the photothermal conversion efficiency and thermal effect of PTT. The thermal effect generated by PTT increases the permeability of the cell membrane, enabling photosensitizers to enter tumor cells more easily. Furthermore, it inhibits DNA damage repair to improve the efficiency of ROS generation, thus enhancing the killing effect of PDT on tumor cells.[10,13–15] However, tumor cell-derived factors might reduce the effectiveness of photothermal therapy by upregulating the expression of heat shock proteins (HSPs) in response to increased temperatures, thereby counteracting the effectiveness of PTT.[16–18] Specifically, HSP90, which belongs to the HSP protein family, can directly protect key client proteins in tumor cells from heat stress damage and reduce tumor cell death; conversely, HSP90 is involved in the regulation of several cellular thermotolerance-related signaling pathways, such as the Raf/MEK/ERK pathway.[19,20] To completely ablate a tumor, the local temperature used for photothermal therapy is often

[a] Cultivation and Construction Site of the State Key Laboratory of Intelligent Imaging and Interventional Medicine, Department of Radiology, Zhongda Hospital, Medical School, Southeast University, Nanjing, 210009, China. E-mail: jsh@seu.edu.cn, xiejb@seu.edu.cn
[b] Department of Microbiology and Immunology, Medical School, Southeast University, Nanjing, 210009, China

† Electronic supplementary information (ESI) available. See DOI: https://doi.org/10.1039/d5tb00071h

‡ These authors contributed equally: Zhiqi Zhang, Fangzheng Tian, Shiwei Lai.

above 50 °C. Such temperatures can result in non-specific thermal diffusion, damaging the healthy tissue around the tumor, and reduce the life quality and survival rate of patients.[21] Moreover, the hypoxic tumor microenvironment (TME) of TNBC facilitates the accumulation of hypoxia-inducible factor-1α (HIF1α) and is stabilized by the chaperone HSP90, while the HIF1α accumulation suppresses the level of ROS production.[22,23] Therefore, there is an urgent need to develop strategies to reduce tumor heat resistance and increase ROS generation, thus improving the efficacy of TNBC therapy.

Inhibition of HSP90 activity promotes the denaturation or unfolding of cellular proteins at high temperatures,[24,25] counteracting the tumor's antipyretic effect and reducing the therapeutic temperatures required for PTT.[26] Moreover, decreased HSP90 activity also reduces the accumulation of HIF1α, further reducing the suppression of ROS by HIF1α. Therefore, blocking the HSP90-HIF1α pathway may decrease the tumor thermoresistance and increase the ROS levels, enhancing the antitumor effect of photothermal therapy. Preclinical studies using HSP90 inhibitors, such as 17-AAG and SNX5442, have shown promising results in enhancing the effect of photothermal and photodynamic therapy in treating malignant tumors.[27–29] In contrast, SNX2112 competitively binds to the N-terminal ATP-binding pocket of HSP90 with higher activity and stronger inhibitory effect. However, their clinical use has been limited due to the low bioavailability and dosing frequency.

Nano-based drug delivery systems (NDDS) enable the encapsulation of multiple drugs for spatially and temporally controlled release,[30–32] offering a potential approach for multidrug combination therapy. In this study, the HSP90 inhibitor SNX2112 and phototherapeutic agent IR825 were self-assembled with the basic framework poly (β-amino esters)–poly (ethylene glycol) (PAE–PEG) to form nano-micelles for treating TNBC. Moreover, studies have shown that photothermal therapy can facilitate the penetration of chemotherapeutic agents to the tumor site,[33–35] so we also introduced chemotherapeutic agents into NDDS to further validate the effect of photothermal therapy on chemotherapeutic agents (Scheme 1). The outer layer of the nano-micelles was modified with cyclic RGD peptides to actively deliver the tumor and increase the tumor penetration by binding with integrin $\alpha_v\beta_3$ expressed on the tumor neovascularization and tumor cell surfaces. In the acidic TME, the nano-micelles underwent pH-responsive dissociation, and the photothermal and photodynamic effect was achieved simultaneously with laser irradiation. SNX2112 downregulated the expression of the HSP90 protein in tumors, inhibiting the HSP90-HIF1α pathway to counteract heat resistance and alleviate ROS suppression, thereby enhancing photothermal and photodynamic therapy. Meanwhile, photothermal therapy led to the accumulation of the chemotherapeutic agent doxorubicin (DOX) in tumors for combined effects. In summary, the nanomicelle carrying SNX2112 was designed to reduce tumor heat resistance and increase ROS generation by suppressing the key HSP90-HIF1α pathway to enhance TNBC treatment.

2. Experimental section

2.1. Materials

DOX was purchased from Aladdin Bio-Chem Technology, Shanghai, China. IR825, poly (β-amino esters)-*block*-poly (ethylene glycol)

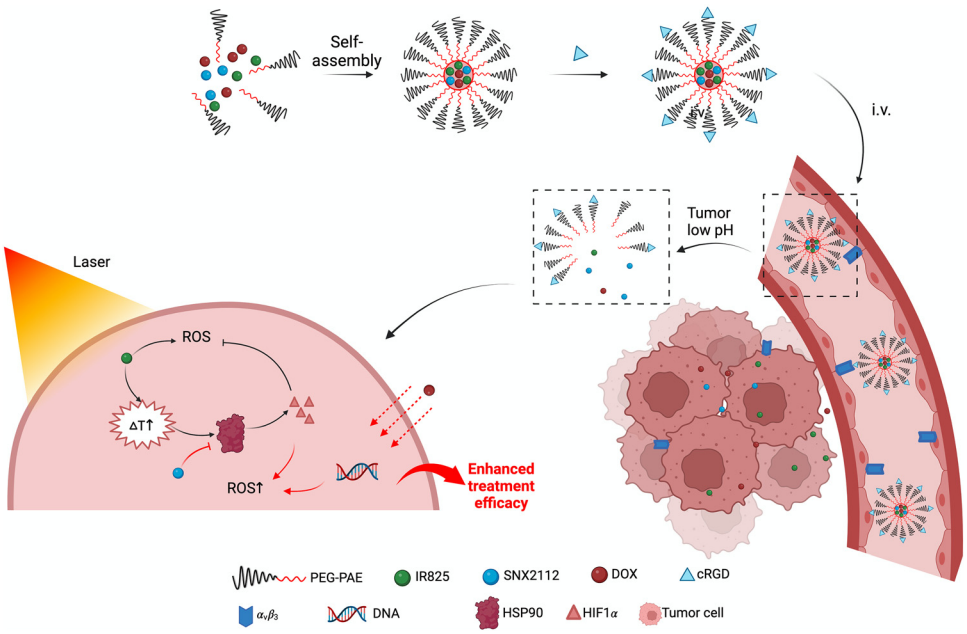

Scheme 1 Schematic of the SIDR structure and strategy for enhanced photothermal therapy against solid tumor. A pH-responsive micelle was self-assembled with SNX2112, IR825, and DOX, followed by conjugating the cRGD peptide that actively transported drugs to the tumor region and released drugs under a low-pH tumor microenvironment. The micelle reduced thermal resistance and increased ROS generation and drug penetration against TNBC effectively by suppressing the HSP90-HIF1α pathway. BioRender.com was used to create the scheme.

(PAE–PEG), and poly (β-amino esters)-*block*-poly (ethylene glycol)-CY7.5 (PAE–PEG-CY7.5) were purchased from RuixiBio, Xian, China. SNX2112 was purchased from MedChemExpress, Shanghai, China. Cyclo(RGDfK)-(ACP)-C was sourced from ChinaPeptides, Shanghai, China. RPMI 1640, fetal bovine serum (FBS), phosphate buffered saline (PBS), penicillin–streptomycin solution and 0.25% Trypsin–EDTA were purchased from Gibco. Dimethyl sulfoxide (DMSO) and 4,6-diamidino-2-phenylindole (DAPI) were purchased from KeyGEN BioTECH, Jiangsu, China. The CCK-8 kit and 2′,7′-dichlorofluorescein diacetate (DCFH-DA) were purchased from Beyotime, Shanghai, China.

2.2. Antibody

Anti-mouse HIF1α rabbit pAb (Cat. No. GB114936-100, 1 : 600) was purchased from Wuhan Servicebio Technology Co., Ltd (Hubei, China). Anti-mouse ERK1/2 rabbit pAb (Cat. No. 11257-1-AP, 1 : 1000) and anti-mouse p-ERK1/2 rabbit pAb (Cat. No. 28733-1-AP, 1 : 1000) were purchased from Proteintech.

2.3. Preparation of SIDR

At room temperature, 500 μg of DOX, 500 μg of SNX2112, 750 μg of IR825, and 2 mg of PEG-PAE (mass ratio = 1/1/1/1.5/4) were simultaneously dissolved in 500 μL of an acetone–ethanol mixed solution (V/V = 1/1). Subsequently, a 5 mL PBS solution (PBS/acetone–ethanol volume ratio = 10/1) was added dropwise into the solution at a constant speed of 1 mL h^{-1} using a dual-channel microinjection pump, while stirring uniformly at 400 rpm with a magnetic agitator. After dripping, the solution was stirred uniformly at 400 rpm in a fume hood overnight to evaporate the organic solvent. Next, cyclo(RGDfK)-(ACP)-C was added to the evaporated solution and stirred for 1 hour at room temperature. The mixture was then loaded into a 3 kDa dialysis bag and dialyzed in pure water for 1 day to remove any unencapsulated drugs. After dialysis, the solution was concentrated using an ultrafiltration tube with a molecular weight cut-off (MWCO) of 3 kDa and washed three times with normal saline to obtain the drug-loaded micellar SIDR solution. The prepared SIDR nano-micelles were stored at 4 °C. The preparation methods of the blank micelles and each control group (IDR, SID, IR, CY7.5-SD, CY7.5-SDR) were the same as that used for SIDR, but the drugs were omitted from the preparation process accordingly.

2.4. Characterization of SIDR

The as-prepared SIDR nano-micelles were stored at 4 °C. The size and morphology of the SIDR nano-micelles were characterized using transmission electron microscopy (TEM; JEM-2100, JEOL Ltd, Japan). The hydrodynamic diameters, characterized by dynamic light scattering (DLS), and the zeta potentials of the TPGS/dc-IR825 nano-micelles in PBS were measured using a zetasizer (90Plus PALS, Brookhaven Instruments, US). To evaluate the stability of the SIDR nano-micelles under different conditions, the nano-micelles were dispersed in PBS, water, and Roswell Park Memorial Institute (RPMI) 1640, and their hydrodynamic sizes were measured by DLS on the 0th, 1st, 3rd, 5th, and 7th day.

2.5. Release profiles of SIDR

To evaluate the pH-triggered release profiles of the SIDR nano-micelles, 2 mL of SIDR nano-micelles was added into a dialysis tube (molecular weight cutoff (MWCO): 1 kDa), which was immersed into 25 mL of PBS at various pH values (6.5 and 7.4). The release profile of DOX was quantified by a fluorescence spectrophotometer based on standard curves.

2.6. Photothermal effect and ROS production of SIDR

600 μL solutions of the PBS and SIDR nano-micelles with different concentrations (5, 10 and 20 μg mL^{-1}) were irradiated with an 808 nm laser (1 W cm^{-2}) for 6 minutes each. During the irradiation, a thermocouple thermometer and an infrared camera (FOTRIC 220S, China) recorded the temperature every 15 seconds. The photothermal stability of SIDR was assessed through four heating–cooling cycles. ROS generation of the SIDR nano-micelles was measured using DPBF as an indicator. The IR825 suspension or SIDR suspension (IR825: 1, 2, 3, 4, 5 μg mL^{-1}) was mixed with 20 μL of DPBF solution, followed by continuous NIR laser irradiation (808 nm, 1 W cm^{-2}). The fluorescence intensity of DPBF was measured at different irradiation time points.

2.7. Cell culture

Murine 4T1 breast cancer cells and Panc02 pancreatic cancer cells were cultured in RPMI 1640 and DMEM (HyClone), respectively, supplemented with 10% (v/v) FBS (Gibco) and 100 IU per mL penicillin–streptomycin (Invitrogen). All cells were cultured at 37 °C in a 5% CO_2 water-jacketed incubator (Thermo Fisher Scientific, Massachusetts, USA). For hypoxic treatment, cells were cultured at 37 °C in an $O_2/CO_2/N_2$ water-jacketed incubator (2% O_2 and 5% CO_2).

2.8. Cellular uptake of SIDR

For fluorescence imaging, 4T1 breast cancer cells were seeded on 6-well cell culture plates and cultured at 37 °C for 24 h. Then, the cells were treated with free DOX or SIDR nano-micelles (DOX: 5 μg mL^{-1}) and incubated for specified time periods. Fluorescence images were captured using an inverted fluorescence microscope (Olympus, Japan). To quantify the cellular uptake of different samples, the cells were treated with free DOX or SIDR nano-micelles (DOX: 5 μg mL^{-1}). After treatment, the cells were harvested, and the intracellular fluorescence intensities were measured using a flow cytometer (NovoCyte 2070, ACEA Bioscience, Inc., USA) at different incubation time points.

2.9. Intracellular ROS measurements

To measure the intracellular ROS level in each group, we utilized DCFH-DA as the ROS probe. DCFH-DA is inherently non-fluorescent and can penetrate the plasma membrane, where it is enzymatically hydrolyzed by intracellular esterases to form dichlorodihydrofluorescein (DCFH). Upon reaction with intracellular ROS, DCFH is converted into the green-fluorescent compound 2′7′-dichlorofluorescein (DCF). Initially,

4T1 cells subjected to various treatments were incubated with 10 μM DCFH-DA for 25 minutes in the dark at 37 °C with 5% CO_2. After washing with PBS, the intracellular fluorescence intensities of DCF were assessed using an inverted fluorescence microscope to assess the ROS levels and measured using a flow cytometer (NovoCyte 2070, ACEA Bioscience, Inc., USA) at different incubation time points.

2.10. Cytotoxicity of SIDR

The cytotoxicity of the SIDR nano-micelles upon NIR light irradiation was evaluated using a CCK-8 assay. 4T1 cells were initially seeded in 96-well cell culture plates and allowed to adhere for 24 hours. Subsequently, cells were treated with different concentrations of SIDR nano-micelles and incubated for an additional 24 hours. After washing with PBS, the cells were exposed to 808 nm light (1 W cm^{-2}). Following another 24-hour incubation period, 10 μL of CCK-8 solution was added to each well and incubated at 37 °C for 2 hours. The optical density (OD) at 450 nm was measured using a microplate reader (IX71, Olympus, Japan), and the cell viability was calculated using the formula: Cell viability (%) = (OD_Sample − OD_Blank)/(OD_Control − OD_Blank) × 100%.

2.11. Animal model

For animal experiments, female BALB/c mice (20 ± 2 g) and C57BL/6 aged five weeks were purchased from Southeast University Medical Center (Nanjing, China). All procedures involving the handling and care of experimental animals were conducted in compliance with the Guidelines for Care and Use of Laboratory Animals of Southeast University and the Regulations for the Administration of Affairs Concerning Experimental Animals of China. To establish the tumor-bearing mouse model, 5×10^6 murine 4T1 breast cancer cells or Panc02 pancreatic cancer cells (suspended in 75 μL of PBS) were subcutaneously injected into BALB/c or C57BL/6 mice.

2.12. *In vivo* optical imaging and bio-distribution

Female BALB/c mice bearing the 4T1 breast cancer tumor (~100 mm^3) were intravenously (i.v.) injected with 200 μL of CY7.5-SDR or CY7.5-SD solution. The mice were placed under deep anesthesia by continuously inhaling a mixture of oxygen with isoflurane (5%). Fluorescence imaging was performed at various time points (1, 3, 6, 9, 12, 24, 48, 72, and 120 hours post-injection) using the IVIS Lumina XRMS Series III system (PerkinElmer) with an excitation wavelength of 780 nm and an emission wavelength of 840 nm. At 48 hours post-injection, the mice were euthanized, and images of the vital organs were captured.

2.13. *In vivo* therapeutic effect

4T1 tumor-bearing mice were randomly divided into nine groups (n = 5): (1) saline: i.v. injected with 200 μL of saline; (2) free DOX: i.v. injected with 200 μL of DOX (2 mg kg^{-1}); (3) free SNX2112: i.v. injected with 200 μL of SNX2112 (2 mg kg^{-1}); (4) SIDR: i.v. injected with 200 μL of SIDR solution (IR825: 3 mg kg^{-1}); (5) laser: i.v. injected with 200 μL of saline with laser irradiation; (6) PDT (SIDR + Laser + Cold): i.v. injected with 200 μL of SIDR solution (IR825: 3 mg kg^{-1}) and cooled by ice during irradiation; (7) PTT (SIDR + Laser + Vc): i.v. injected with 200 μL of SIDR solution (IR825: 3 mg kg^{-1}) and injected Vc solution intra-tumoral before irradiation; (8) IDR + Laser: i.v. injected with 200 μL of IDR solution with laser irradiation; (9) SIDR + Laser: i.v. injected with 200 μL of SIDR solution with laser irradiation. Panc02 tumor-bearing mice were randomly divided into 8 groups, excluding the 'radiation-only' group. Laser irradiation was performed using an 808 nm laser (1 W cm^{-2}, keep the temperature at 42 degrees for 3 min) at 48 hours post injection. The temperature changes at the tumor areas were recorded using an infrared thermal imager. Tumor volumes and the weights of mice were monitored every three days for three weeks. Tumor volumes were calculated using the formula: (width^2 × length)/2. To further evaluate the anticancer outcomes, 4T1 tumor-bearing mice were sacrificed on day 14, and their tumors were excised and fixed in 4% paraformaldehyde solution. The fixed tumors were then embedded in paraffin, sectioned, and stained with hematoxylin and eosin (H&E) and TdT-mediated-dUTP nick end labeling (TUNEL) according to standard protocols. The expression of HSP90 and HIF1α was detected by immunohistochemical staining. To detect collagen in the tumor tissues, paraffin-embedded tumor slides were stained with Masson's trichrome stain by the UNC Tissue Procurement Core. Images of the slides were captured using a Nikon microscope with a 20× objective. To evaluate the systemic toxicity of SIDR, mice were sacrificed on day 14, and their major organs (heart, liver, spleen, lung, and kidney) were excised and processed as described above.

2.14. Hematological indices and biochemical analyses

Blood samples were collected from treated mice (without tumor inoculation) at days 1, 7, 14, and 30 post-injections. The blood cells were analyzed using an automatic hematology analyzer (BC-2800Vet, Mindray, China). Biochemical analyses were performed using an automated biochemical analyzer (SMT-100 V, Seamaty, China).

2.15. Statistical analysis

Results were expressed as mean ± SD. For comparison within two groups, an unpaired two-tailed t-test was used. For comparison among multiple groups, one-way analysis of variance (ANOVA) was used. GraphPad 7.0 was used for statistical analysis. A P value of less than 0.05 was considered as a significant difference.

3. Results and discussion

3.1. Preparation and characterization of pH-responsive SIDR

Amphiphilic polymer poly (β-amino esters)–poly (ethylene glycol)–maleimide (PAE–PEG–MAL) was employed to encapsulate three hydrophobic drugs (near-infrared (NIR) dye IR825, HSP90 inhibitor SNX2112 and chemotherapy drug DOX) by spontaneous micellization in an aqueous solution, forming

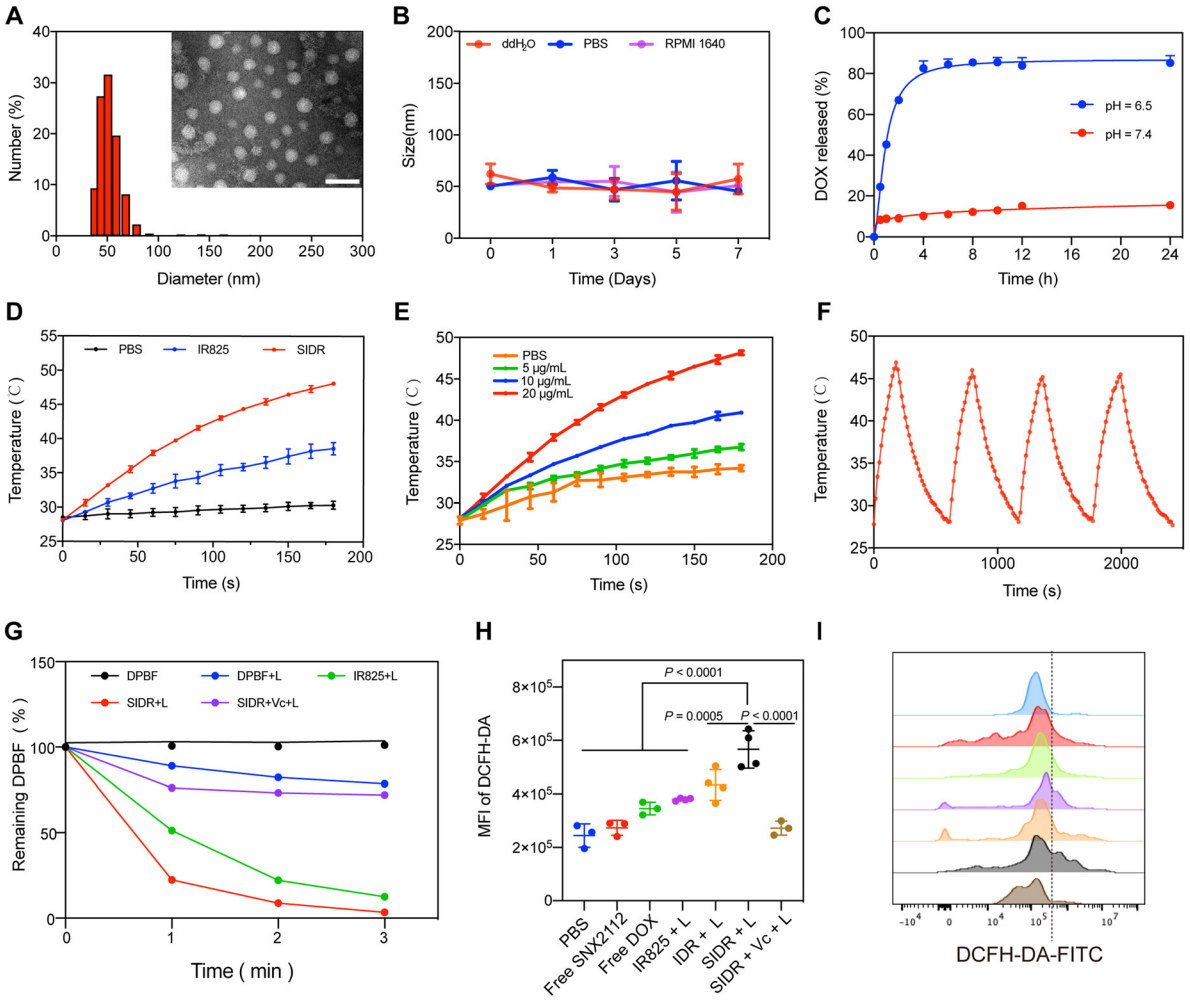

Fig. 1 Characterization of SIDR nano-micelles. (A) Dynamic light scattering (DLS) analysis of SIDR. Inset: The transmission electron microscopy (TEM) image (scale bar = 100 nm). (B) The stability of SIDR in different environments (ddH_2O, PBS and RPMI 1640) for 7 days. (C) DOX release profiles from SIDR nano-micelles under different pH conditions (pH = 6.5 and 7.4). (D) The photothermal profiles of IR825 and SIDR nano-micelles after laser irradiation (IR825 concentration: 20 μg mL^{-1}). (E) The photothermal profiles of SIDR with various IR825 concentrations upon 808 nm irradiation. (F) The photothermal capability of SIDR nano-micelles over four laser on/off cycles (IR825 concentration: 20 μg mL^{-1}). (G) Relative absorbance of DPBF at 420 nm during ROS detection using an DPBF assay after different treatments (IR825 concentration: 5 μg mL^{-1}. Vc: 1 mM). (H) Representative flow cytometry histogram and (I) quantitative mean fluorescence intensities (MFIs) derived from flow cytometric results in intracellular ROS detection by DCFH-DA. L: with laser irradiation, 808 nm, 1 W cm^{-2}. n = 3. Statistical significance was calculated using one-way ANOVA with Fisher's LSD test.

nano-micelles SNX2112@IR825@DOX-cRGD (SIDR), with the polypeptide cRGD modified in the outer layer. The formation of the SIDR nano-micelles was verified by transmission electron microscopy (TEM) and dynamic light scattering (DLS) analysis, revealing spherical and homogeneous micelles with a size of about 50 nm (Fig. 1A), characterized by a narrow size distribution and zeta potential of 21 mV (Fig. S1A, ESI†). Moreover, the stability of SIDR was evaluated by incubating them in different environments such as PBS (pH 7.4), ddH_2O, and RPMI-1640 cell medium. The results showed that SIDR was well-dispersed and exhibited excellent stability with minimal size change during the 7-days treatment in different environments (Fig. 1B and Fig. S1B, ESI†). To exemplify the self-assembly mechanism of the nanomicelles, the TEM and DLS of Free DOX, DOX micelles (micelles only loaded with DOX), SD micelles (micelles loaded with SNX2112 and DOX), ID micelles (micelles loaded with IR825 and DOX), and SID (micelles loaded with SNX2112, IR825 and DOX) were examined. The TEM results showed that free DOX presented a free state and did not take shape, which may due to the free DOX being so small that it is not observable under the TEM. After encapsulating DOX into the nanomicelles, a round shape with a diameter of about 15 nm was observed. Upon co-encapsulation of SNX2112 or IR825, the diameter of the nanomicelles increased until round micelles with a diameter of 50 nm were visible after encapsulating all three drugs (SNX2112, DOX, and IR825) into the nanomicelles (Fig. S2, ESI†).

Due to its tertiary amine moiety, the PAE part can be protonated at low pH. This increases its hydrophilicity, leading to a shift in the micelle structure, which allows for the release of the drug.[36] Therefore, the release profiles of DOX from SIDR in different pH environments (pH = 6.5, pH = 7.4 PBS) were

investigated to ensure drug release under acid conditions. Under physiological conditions (pH = 7.4), the drug release was significantly lower compared to that at pH = 6.5 (tumor tissue microenvironment) (Fig. 1C), with only about 1/6th of the release observed in the acid environment within 24 hours. However, the release rate of SIDR at pH = 6.5 was markedly accelerated, with 80% of DOX released within 24 hours. This property allows for specific drug release to occur in the acidic TME, while minimized leakage occurs under normal physiological conditions, thereby reducing systemic toxicity.

3.2. High photothermal conversion and ROS productivity of SIDR

Owing to the strong NIR absorption of SIDR, the micelle can serve as a PTT agent for tumor treatment. Compared to the same concentration of IR825 alone, the temperature of SIDR increased more noticeably within 3 minutes under the same irradiation (808 nm, 1 W cm^{-2}) (Fig. 1D and Fig. S3A, ESI†). Moreover, in the SIDR group, the temperature increases showed an obvious IR825 concentration-dependence and time-dependence upon the same irradiation, whereas PBS showed minimal changes (Fig. 1E and Fig. S3B, ESI†). Organic NIR-absorbing dyes generally tend to photodegrade under continuous laser irradiation, leading to a loss of their photothermal properties.[17] However, SIDR showed good photostability with only a slight decrease in its NIR absorbance after 40 minutes of laser irradiation (Fig. 1F), indicating that the formation of nano-micelles effectively mitigates the photodegradation of IR825.

Under laser irradiation, SIDR converts the oxygen into reactive oxygen species (ROS), many of which are the singlet oxygen ($^1O_2$).[37] Then, the production of $^1O_2$ was examined using the $^1O_2$ probe diphenylisobenzofuran (DPBF). In the presence of $^1O_2$, DPBF undergoes a structural change, leading to a decrease in absorbance at its ultraviolet absorption peak (410 nm). Therefore, the degree of attenuation is indicative of the $^1O_2$ content. A significant decrease in the absorbance value of DPBF was observed with SIDR under laser irradiation compared to DPBF alone under laser (Fig. 1G). This result suggests that SIDR generates a substantial amount of $^1O_2$ under laser irradiation. When vitamin C (Vc), a strong reducing agent,[6] was co-cultured with SIDR, the attenuation of the DPBF absorbance was reduced under laser, confirming that the decrease in the DPBF absorbance is indeed due to the production of $^1O_2$. Furthermore, a positive correlation was observed between the decrease in the DPBF absorbance and the concentration of IR825 in SIDR (Fig. S4, ESI†).

In addition, the intracellular ROS levels were detected using the ROS probe dichlorofluorescein diacetate (DCFH-DA). Fluorescence imaging (Fig. S5, ESI†) and flow cytometry (Fig. 1H and I) analysis showed that cells in the 'free SNX2112, free DOX' group and 'free IR825 + L' group exhibited weak fluorescence due to insufficient ROS generation. In contrast, the 'IDR + L' group, which combined photochemotherapy, showed stronger fluorescence. Remarkably, cells treated with SIDR exhibited the strongest green fluorescence after laser irradiation. This enhanced ROS generation in the SIRD-treated cell may be attributed to the inhibition of HSP90 by SNX2112, resulting in increased ROS production during photochemotherapy. Importantly, this effect can be blocked by Vc (1 mM). These results together indicate that SIDR is more effective in generating ROS compared to the control groups, highlighting its potential to enhance the efficacy of photodynamic therapy. These results suggest that SIDR possesses excellent photoproperties for cancer treatment.

3.3. Cytotoxicity and penetration of SIDR

The $\alpha_V\beta_3$ receptor is a cell-surface receptor of the cRGD peptide and is often overexpressed on tumor neovascularization and tumor cells, such as breast cancer cells and pancreatic cancer cells.[38] cRGD peptide-based nano-micelles can specifically bind to $\alpha_V\beta_3$, followed by internalization into the cells.

To investigate the receptor-mediated targeted ability of nano-micelles, SIDR was incubated with mouse 4T1 breast cancer cells and observed under a fluorescence microscope. Strong fluorescence was clearly observed from the 4T1 breast cancer cells treated with the 'SID + L' and 'SIDR + L' groups for 4 hours, while little fluorescence was detected in the 'free DOX' group, suggesting that the formation of nanostructures enhanced the internalization of drugs (Fig. 2A and Fig. S6, ESI†). Moreover, the fluorescence signal of cells in the SID + L group was higher than that in the SID group without irradiation, indicating that phototherapy can facilitate the penetration of chemotherapeutic agents. Subsequently, the results were further analyzed by flow cytometry (Fig. 2B). The quantitative mean fluorescence intensity (MFI) of the 'SID + L' group was lower than that for the 'SIDR + L' group, confirming the enhanced internalization of nano-micelles through the receptor-related active targeting mechanism. Fluorescence imaging at different time points and flow cytometry analysis of the MFI of the 4T1 breast cancer cells showed that the cell uptake of the SIDR nano-micelles was positively time-dependent (Fig. S7, ESI†).

In addition, the results were further confirmed in a mice model. Histological analyses were performed on the 4T1 tumor-bearing mice treated with saline, free DOX, SID + L and SIDR + L. Compared to the 'free DOX' group, there was an increased local accumulation of DOX in tumors in the SID group. Notably, the SIDR group specifically took up more DOX at the tumor site (Fig. 2C). These results indicate that phototherapy can facilitate the penetration of chemotherapeutic agents, and SIDR is an excellent drug delivery system that is capable of carrying drugs into tumor cells.

Next, the laser-activated cytotoxicity of the SIDR was assessed *in vitro*. The effects of SIDR on TNBC cell lines (4T1 breast cancer cells) and pancreatic cancer (PC) cell lines (Panc02 pancreatic cancer cells) were investigated to verify that SIDR can work in different solid tumors. The cell viability exceeded 90% after incubating 4T1 breast cancer cells (Fig. S8A, ESI†) and Panc02 pancreatic cancer cells (Fig. S8B, ESI†) with blank micelles (the micelles without drugs), indicating the excellent bio-safety of the polymer hydrophobic shell. The phototoxicity of all other groups was dose-dependent (Fig. 2D).

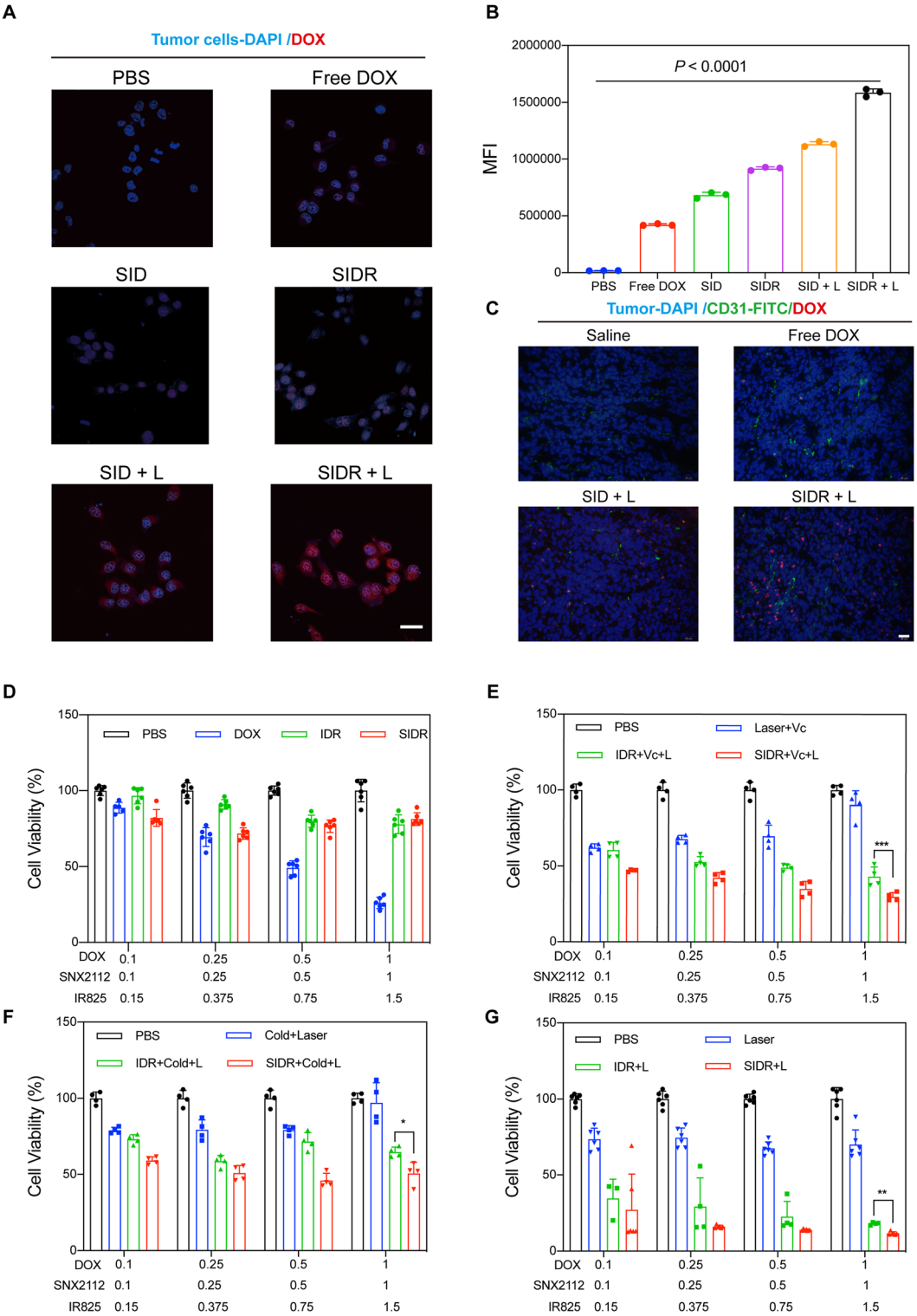

Fig. 2 Cell uptake and cytotoxicity promoted by SIDR in 4T1 cells. (A) Fluorescence images of 4T1 cells incubated with free DOX, SID, SIDR, SID + L and SIDR + L (scale bar = 30 μm). (B) Quantitative mean fluorescence intensities (MFI) derived from the flow cytometric results in (A). (C) Representative images of DOX accumulated in the 4T1 tumor tissue (scale bar = 20 μm, red: DOX, green: CD31, and blue: DAPI). (D)–(G) Relative viability of 4T1 cells with different treatments (L: with laser irradiation, 808 nm, 1 W cm^{-2}, 3 min; unit: μg, and medium volume: 200 μL), which indicate (D) the effect of micelles only, (E) PTT, (F), and (G) micelles under irradiation. Vc: 1 mM, L: with laser irradiation, 808 nm, 1 W cm^{-2}. $n \geq 3$, $^{*}P < 0.05$, $^{**}P < 0.01$, and $^{***}P < 0.001$. Statistical significance was calculated using one-way ANOVA with Fisher's LSD test.

There was no significant difference in the efficacy of SIDR and IDR in the absence of laser irradiation. This is possibly due to the inability of *in vitro* experiments to fully simulate the complex microenvironment (such as low pH) of tumors *in vivo*. Meanwhile, the cold environment and Vc were used to counteract the role of thermogenesis and ROS, respectively, for our assessment of the SIDR single efficacy. Compared with the IDR group, the photothermal killing rate of SIDR was increased by about 20% (Fig. 2E), and the ROS killing rate of SIDR was increased by about 14% (Fig. 2F). It is worth noting

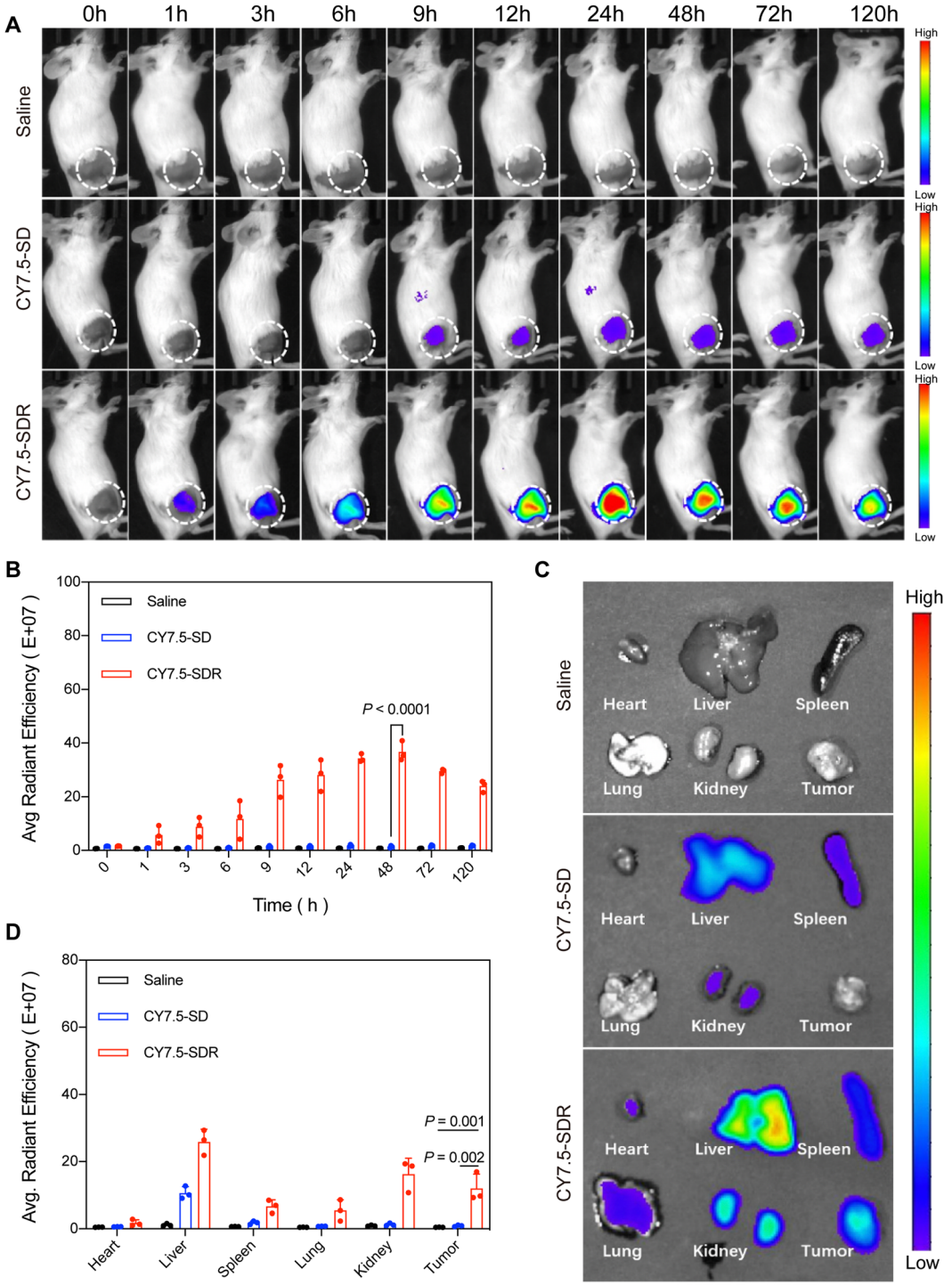

Fig. 3 Assessment of the penetration ability by SIDR *in vivo* and *ex vivo*. (A) *In vivo* fluorescence images of 4T1 tumor-bearing mice taken at different time points after the intravenous injection of saline, CY7.5-SD, CY7.5-SDR. (B) Average fluorescence intensities of tumor areas, as partially shown in A. (C) *Ex vivo* fluorescence images of major organs and tumors excised from mice at 48 h after i.v. injection with saline, CY7.5-SD, and CY7.5-SDR. (D) Average fluorescence intensities of tumor areas, as partially shown in C. $n = 3$. Statistical significance was calculated using one-way ANOVA with Fisher's LSD test.

that the killing effect of SIDR on cells after irradiation was significantly better than that of IDR, indicating that SNX2112 can significantly improve the cytotoxicity of SIDR on cells (Fig. 2G). Similar results were observed in Panc02 pancreatic cancer cells, confirming the efficacy of SIDR in both cell lines (Fig. S9, ESI†).

3.4. Accumulation and biodistribution of SIDR in tumor models

RGD peptides achieve targeted delivery by specifically binding to integrin $\alpha_v\beta_3$ receptors. Integrin receptors are highly expressed on the surface of tumor neovascular endothelial cells and solid tumors such as TNBC, while their expression is low in normal tissues.[39,40] PEG-PAE is protonated in the acidic microenvironment of tumors, which results in the disruption of micellar structure and release of the drug. RGD-mediated active targeting ensures that the micelles are efficiently enriched at the tumor site, and pH sensitivity triggers the release of the drug thereafter. Through the active targeting of RGD and the intelligent response of the pH sensitivity, the nanomicelles were able to adapt to the characteristics of the tumor microenvironment for efficient drug delivery and controlled release.

The encapsulation of the peripheral polymer micelles and the hydrophobic aggregation of IR825 itself could lead to aggregation fluorescence quenching.[41,42] As such, the concentration of drug aggregation reflected by the fluorescence signal of the nano-micelles was far less than the actual concentration. To address this, we used polymer CY7.5-PEG2000-PAE to prepare nano-micelles as fluorescent imaging substitutes (CY7.5-SDR, CY7.5-SD).

The fluorescence images of saline, CY7.5-SD and CY7.5-SDR were monitored at different time points after being intravenously injected into 4T1 tumor-bearing mice to decode the biodistribution behavior of the nano-micelles *in vivo*. The fluorescence signal was observed at the tumor site for the CY7.5-SDR group within 1 hour (Fig. 3A). Moreover, the fluorescence intensity at the tumor site gradually increased within 48 hours after injection. Even at 120 hours post-injection, the tumor exhibited significant fluorescence, indicating the excellent tumor enrichment and long-term tumor retention of CY7.5-SDR, as evidenced by the fluorescence quantitative analysis (Fig. 3B). Then, mice were sacrificed at 48 hours post-injection to harvest the tumor tissues and organs for *in vitro* fluorescence imaging (Fig. 3C). The fluorescence signal of the control group was negligible. In contrast, the CY7.5-SDR group showed an intense fluorescence signal in the tumor tissue, with a 13.4-fold higher accumulation in the tumor compared to the group without cRGD peptides. The quantitative analysis data confirmed this result (Fig. 3D). The outstanding tumor-targeting ability of CY7.5-SDR or SIDR was closely related to the modified RGD peptide, which prolonged blood circulation, achieved the targeting effect, and significantly enhanced tumor penetration.

3.5. *In vivo* photothermal conversion properties and antitumor efficacy of SIDR

The photothermal conversion properties of SIDR were further investigated 48 hours post-injection *in vivo*. Since TNBC and PC have multiple aspects in common (*e.g.*, both have dense fibrotic mesenchyme, which significantly impedes drug penetration[43,44]), both produce large amounts of lactic acid, resulting in an acidic tumor microenvironment.[45,46] Furthermore, both exhibit hypoxic characteristics, promoting the expression of factors such as HIF1α.[47] These features led to further use of the PC mouse model in subsequent studies to further validate the therapeutic effect of SIDR.

For 4T1 or Panc02 tumor-bearing mice injected with SIDR, the tumor temperature rapidly increased after irradiation, reaching the highest temperature over 45 °C (Fig. 4A and B), which meets the requirements of tumor photothermal therapy. By contrast, no obvious change in tumor temperature was observed in the saline group. The results from the Panc02-tumor models further confirmed these findings (Fig. 5A and B), suggesting that SIDR can effectively induce hyperthermia in tumor tissues. Furthermore, an infrared thermal imager was used to analyze the 'SIDR + L' group in addition to the 'Vc-treated' or 'Cold-treated' groups. The 'SIDR + L + Cold' group, which uses cold treatment to prevent the temperature from rising, represents the PDT group, while the 'SIDR + L + Vc' group, which uses Vc to block ROS production, represents the PTT group.

The results showed that in the 4T1 and Panc02 tumor models, the local temperature change of the tumor in the photodynamic group was nearly identical to that of the saline group ($P > 0.05$). Meanwhile, the local change of the tumor in the photothermal group was similar to that of the 'SIDR + L' group ($P > 0.05$), and significantly different from that of the saline group ($P < 0.0001$). This suggests that the local change of the tumor induced by SIDR was mainly caused by the photothermal effect.

In subsequent treatment trials, the local temperature of the tumor was kept at 42 °C for 3 minutes to reduce damage to healthy tissues from thermal injury.

The *in vivo* synergistic therapeutic efficiencies of SIDR nanomicelles were assessed using 4T1 and Pan02 tumor-bearing mice (Fig. 4C and 5C). For the saline or only laser-treated mice, the tumor volume grew rapidly during treatment. Compared with the 'free DOX' group, the 'SIDR-treated' group without laser irradiation showed better tumor inhibition (Fig. 4D). This may be related to the tumor targeting and high tumor accumulation of nano-micelles, indicating that the nano-micelles can effectively enhance the anticancer effect of chemotherapy drugs. Compared to PTT or PDT monotherapy, the combination of PTT and PDT was observed to be more effective in inhibiting tumor growth (Fig. 4D group f or g *v.s.* group h). Notably, compared with the IDR nano-micelles without the HSP90 inhibitor SNX2112, the tumor inhibition effect was more pronounced in the SIDR group after irradiation. This indicates that the HSP90 inhibitor plays an important role in enhancing the efficacy of tumor phototherapy (Fig. 4D group h *vs.* group i). More promisingly, the tumor volume and weight in the 'SIDR after laser' group measured at the endpoint (14 days post-treatment) were the smallest and even close to zero (Fig. 4E). Hematoxylin and eosin (H&E) staining of tumor slices confirmed these results, showing that the tumor tissue of 'SIDR

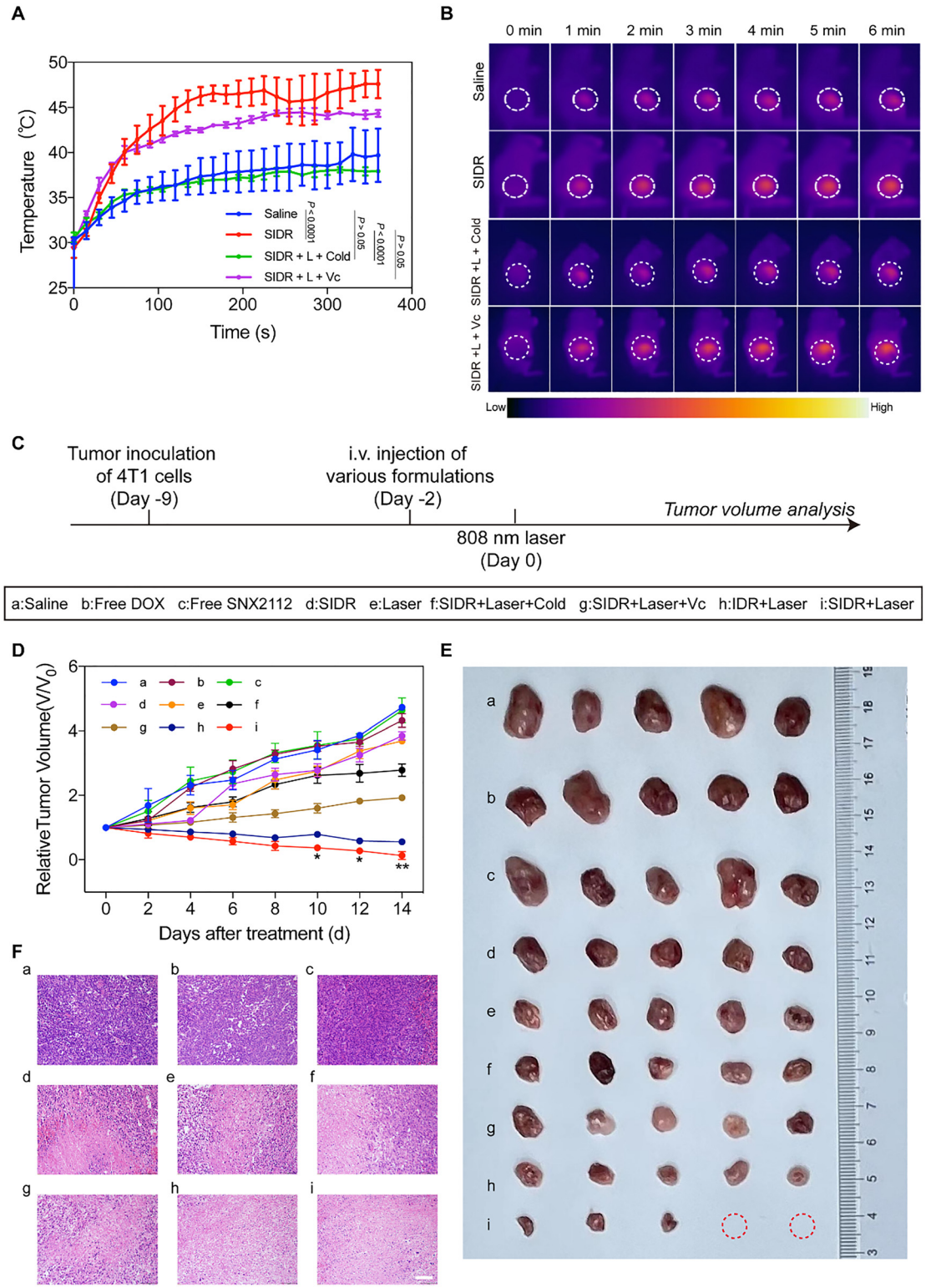

Fig. 4 *In vivo* thermal imaging and antitumor evaluation in 4T1 tumor-bearing mice. (A) Temperature changes and (B) thermal images of tumor regions after intravenous injection with saline, SIDR, SIDR + cold or SIDR + Vc upon continuous laser irradiation for 6 min, $n = 3$. (C) Schematic of the treatment regimen. The box shows grouping information. (D) Tumor growth curves for different groups of mice after various treatments (the significance of the data is group h *v.s.* group i, $n = 3$, the temperature was kept at 42 °C for 3 min). (E) Tumor morphology of mice at day 14 after different treatments ($n = 5$, keep the temperature at 42 degrees for 3 min). (F) H&E-stained tumor slices for each treatment group at day 14 (scale bar = 100 μm). $^{*}P < 0.05$, $^{**}P < 0.01$. L: with laser irradiation, 808 nm, 1 W cm^{-2}. Statistical significance was calculated by the two-sided *t* test in B, and one-way ANOVA with Fisher's LSD test in D.

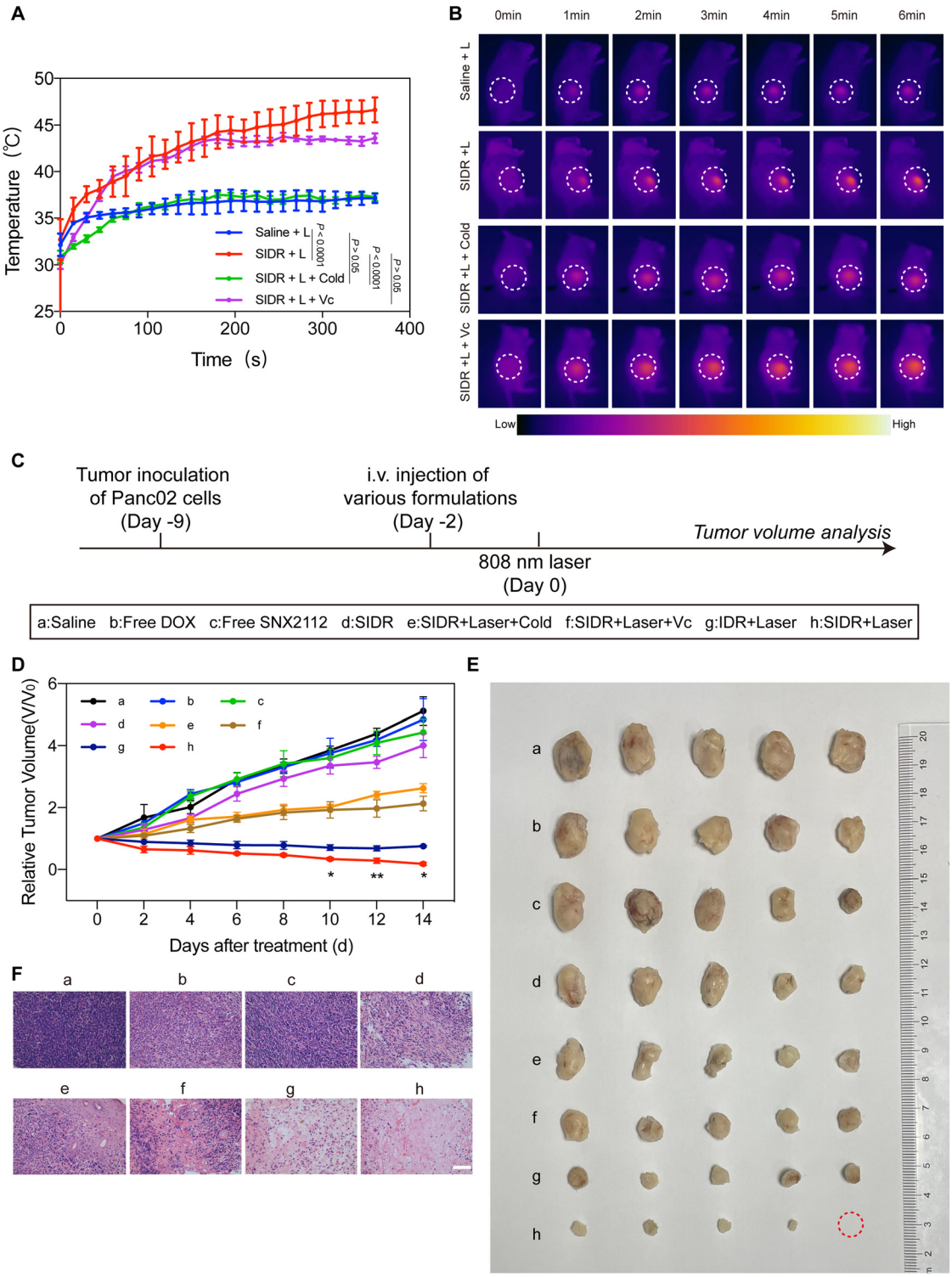

Fig. 5 *In vivo* thermal imaging and antitumor activity evaluation in Panc02 tumor-bearing mice. (A) Temperature changes and (B) thermal images of tumor regions after intravenous injection with saline, SIDR, SIDR + Cold or SIDR + Vc upon continuous laser irradiation (808 nm, 1 W cm^{-2}) for 6 min, n = 3. (C) Schematic of the treatment regimen. The box shows grouping information. (D) Tumor growth curves in different groups of mice after various treatments (the significance of the data is group g *vs.* group h, n = 5). (E) Tumor morphology of mice at day 14 after different treatments (n = 5, the temperature was kept at 42 °C for 3 min). (F) H&E-stained tumor slices for each treatment group at day 14 (scale bar = 100 μm). *$P < 0.05$, **$P < 0.01$. L: with laser irradiation, 808 nm, 1 W cm^{-2}. Statistical significance was calculated using two-sided t test in B and one-way ANOVA with Fisher's LSD test in D.

after laser' treated mice was completely eradicated (Fig. 4F). Similar results were obtained in the Panc02 tumor-bearing mice model (Fig. 5D–F). TUNEL staining also showed a large sheet of green fluorescence in the 'SIDR after laser' group

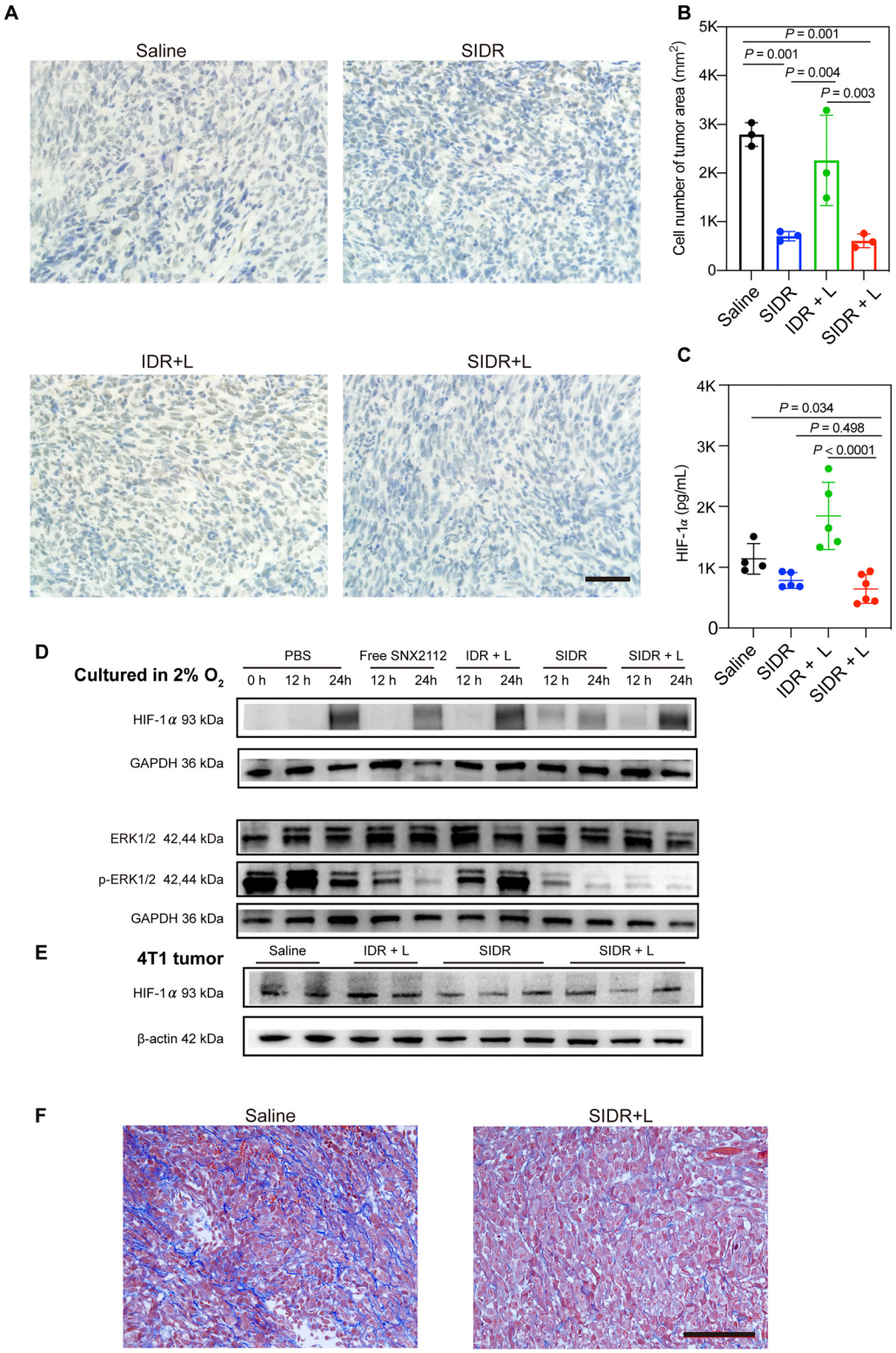

Fig. 6 SIDR inhibited the HSP90-HIF1α pathway and reduced the fiber barrier. (A) Representative immunohistochemistry (IHC) images and qualification (B) of HIF1α in tumor tissue sections 14 days after injection of different treatments in 4T1 tumor-bearing models, n = 3, scale bar = 100 μm. (C) HIF1α detection through enzyme-linked immunosorbent assay (ELISA) using 4T1 tumor, n = 5. (D) HIF1α, ERK1/2 and p-ERK1/2 detection using western blot (WB) using 4T1 cells in 2% O_2 conditions. (E) HIF1α detection *via* WB using 4T1 tumor 14 days after injection of different treatments in 4T1 tumor-bearing models. 4T1 tumor bearing-mice: saline and IDR + L treated mice (n = 4), SIDR treated mice (n = 5), SIDR + L treated mice (n = 6). (F) Masson staining in tumor tissue sections 14 days after injection of different treatments in 4T1 tumor-bearing models, scale bar = 100 μm. Statistical significance was calculated using one-way ANOVA with Fisher's LSD test.

(Fig. S10, ESI†). These results indicate that SIDR-mediated synergistic photothermal, photodynamic and chemotherapy can efficiently inhibit tumor growth and almost achieve complete tumor regression.

3.6. Toxicity and safety evaluation

The long-term retention of SIDR *in vivo* was assessed through hematological indices and biochemical analysis of non-tumor-bearing mice treated with SIDR on days 1, 7, 14, and 30 post-injection. No significant differences were observed in the values of white blood cells (WBC), red blood cells (RBC), hemoglobin (HGB), mean corpuscular volume (MCV), mean corpuscular hemoglobin (MCH), mean corpuscular hemoglobin concentration (MCHC), glutamate pyruvate transaminase (ALT), aspartate aminotransferase (AST), urea and creatinine (CREA) between the reference values and those of mice treated with SIDR (Fig. S11A, ESI†). On day 14, the main organs of the mice were harvested and stained with H&E to investigate the potential *in vivo* toxicity (Fig. S11B, ESI†). All treatment groups exhibited no evident pathological abnormalities in the main organs, indicating that SIDR did not induce obvious systemic toxicity. *In vivo* toxicity of SIDR was further investigated by monitoring the body weight change of the mice. Throughout the study period, mice in all groups showed no loss of body weight (Fig. S11C, ESI†), indicating acceptable biocompatibility of all treatments. Overall, these results clearly demonstrate that SIDR has the potential to be a safe nano-micelle for cancer therapy.

3.7. SIDR enhances the effect of photothermal combined photodynamic therapy by suppressing the HSP90-HIF1α pathway

To further investigate the mechanism of SIDR for solid tumors, we examined its impact on the HSP90-HIF1α pathway. HSP90 is a key molecule involved in client protein folding and function within cells.[48] Many HSP90 client proteins promote tumor growth, tissue remodeling, and metastasis.[49] One such client protein, HIF1α, actively participates in tissue remodeling[25,50] and is overexpressed in desmoplastic tumors, such as TNBC and PC, which is characterized by abundant fibrous tissue infiltration around the tumor.[25] Clinical studies have shown elevated hypoxia levels in these tumors, quantified by HIF1α expression, which is significantly correlated with poor prognosis.[51] This hypoxic microenvironment promotes collagen synthesis and accumulation,[25] leading to desmoplastic tumors that are more resistant to therapy.[41,52]

Therefore, the expression of HSP90 client proteins was investigated, including HIF1α, ERK1/2 and ERK1/2 phosphorylated forms (p-ERK1/2). Their expression was used to reflect the activity of HSP90.[24,29] HIF1α expression was firstly examined using immunohistochemistry (IHC) (Fig. 6A and B and Fig. S12, ESI†) and enzyme-linked immunosorbent assay (ELISA) (Fig. 6C and Fig. S13, ESI†). The 'saline' and 'IDR + L' groups showed high HIF1α expression in tumor tissue derived from the 4T1 and Panc02 tumor-bearing mice, which was significantly alleviated by irradiated or non-irradiated SIDR treatment. Moreover, western blot (WB) analysis further revealed that treatment with free SNX2112 inhibited HSP90 activity, and decreased HIF1α accumulation and p-ERK1/2 levels in 4T1 cells. Meanwhile, encapsulation of SNX2112 into the SIDR nano-micelle did not affect the effect (Fig. 6D). The results were further validated in 4T1 and Panc02 tumor tissues (Fig. 6E and Fig. S14 and S15, ESI†).

Collagen accumulation by Masson staining was also assessed. The 'SIDR + L treated' groups exhibited a significant decrease in collagen content compared to the untreated group (Fig. 6F and Fig. S16, ESI†), which is beneficial for desmoplastic tumors.[53] These results suggested that SIDR can inhibit the HSP90-HIF1α pathway and induce stromal remodeling of TNBC and PC. In conclusion, SIDR enhances the combined effect by inhibiting the HSP90-HIF1α pathway, reducing heat resistance, increasing ROS production, and breaking down the fibrous barrier around tumors to improve drug penetration and therapeutic efficacy.

4. Conclusion

We have developed a pH-responsive nano-micelle that co-encapsulates HSP90 inhibitors (SNX2112), chemotherapeutic agents (DOX), and photosensitizers (IR825) for effective TNBC therapy. Despite advancements in cancer treatment, patients with TNBC often face challenges in achieving complete remission. The presence of a tumor barrier, including collagen, limits the penetration of chemotherapeutic agents within the tumor. While photothermal and photodynamic therapy have shown promise in improving tumor permeability, they also present new challenges. During photothermal therapy, tumors can develop a defense mechanism by upregulating HSP90 expression. This can lead to resistance to therapy, necessitating longer or more intense light exposure. As a result, localized temperatures can increase to values above 50 °C,[21,54] which can be harmful to the surrounding healthy tissues. Additionally, HSP90 is a molecular chaperone, and its client proteins contribute to the inhibition of therapeutic effects and promotion of tumor proliferation in the tumor microenvironment. For example, HIF1α, a client protein of HSP90, can affect ROS levels and protect tumor cells. Combining HSP90 inhibitors with photosensitizers represents a promising approach to enhance the anti-TNBC efficacy. By targeting HSP90, this nano-micelle system aims to overcome resistance mechanisms and improve the effectiveness of therapy against solid tumors in a bio-safe and effective manner at a mild temperature (42 °C).

Current studies have designed diagnostic-integrated, multi-mechanism synergistic nanomicelles capable of triggering drug release or size conversion *via* pH, ultrasound, or photothermal pathways for precision diagnosis and treatment.[55–58] In this study, SIDR nano-micelles were bound to cRGD-targeted peptides *via* pH-responsive release, reducing the off-target toxicity of the drug. In addition, by inhibiting the HSP90-HIF1α pathway, the chemotherapeutic effect of DOX and the photothermal effect of IR825 were enhanced, thus reaching the therapeutic effect on TNBC at mild temperatures. We used TNBC as the first therapeutic model. Meanwhile, to demonstrate the broad applicability of SIDR, a model of PC was established. *In vivo* and

ex vivo imaging studies demonstrated that SIDR rapidly detected $\alpha_v\beta_3$ on neovascularization and TNBC cells following intravenous injection, thereby facilitating the entry of SNX2112, DOX, and IR825 into the TME. It dramatically increased tumor accumulation in multiple tumor xenograft models of the CY7.5-SDR compared to the CY7.5-SD group. cRGD-targeted peptide and pH-responsive properties augmented the specificity of the nano-micelle, and SNX2112 was efficiently released from the nano-micelle in the acidic TME without compromising its inhibitory effect on HSP90. Thus, the ROS-generating and photothermal conversion properties of IR825 were enhanced and the accumulation of DOX was promoted within tumors. The results of the antitumor experiments in the TNBC and PC animal models demonstrated that SIDR + L treatment profoundly inhibited the tumor growth. The results of IHC, WB, and ELISA showed that SIDR treatment inhibited the activity of HSP90 and reduced the aggregation of HIF1α in tumors. Thus, engineered SIDR can effectively target solid tumors and enhance photochemical potency by combined PDT and PTT efficacy to suppress primary tumor growth. NanoDDS can be activated by increased delivery and specificity of chemotherapeutic agents, as evidenced by the effective eradication of solid tumor therapy by SIDR in preclinical models.

Nano-micelles, with their drug-loading maneuverability and pH-sensitive properties, provide a versatile platform for drug co-delivery and controlled drug release. This platform reduces drug leakage in the circulation and avoids toxic effects, without requiring complex custom modifications or alterations. In addition to SNX2112, DOX and IR825, this smart nano-system can administer a variety of other therapeutic drugs. The nano-micelles can co-encapsulate multiple drugs, allowing different drugs to act synergistically to improve therapeutic efficacy.

In conclusion, our study provides an improved approach *via* combined therapy to enhance the penetration of chemotherapeutic agents into solid tumors and augment photothermal and photodynamic therapy using HSP90 inhibitors. These findings may be promising for other types of malignancies therapies.

Author contributions

Z. Z., F. T. and S. L. (Shiwei Lai) conducted the synthesis, characterization, cell studies, animal experiments, data analysis, and wrote the manuscript. X. X., M. Z., Z. H., S. L. (Siyu Li), J. Z. and X. Y. contributed to the data analysis and discussed the data. J. X. and S. J. commented on and revised the manuscript and supervised the project.

Ethics approval

All applicable international, national, and/or institutional guidelines for the care and use of animals were followed.

Consent to participate

Not applicable.

Data availability

The authors declare that all data supporting the findings of this study are available within the paper and its ESI† files.

Conflicts of interest

The authors declare no competing interests.

Acknowledgements

Funding This study was supported by the National Key R&D Program of China (2021YFF0501504 and 2021YFA1101304 for S. J. and 2022YFE0116700 for J. X.) and the National Natural Science Foundation of China (NSFC, No. 82330060, 92359304 and 82427803 for S. J., 82372023, 82172010 for J. X. and 82402355 for X. X.).

References

1 J. E. Abraham, K. Pinilla and A. Dayimu, *et al.*, The PARTNER trial of neoadjuvant olaparib in triple-negative breast cancer, *Nature*, 2024, **629**, 1142–1148.
2 D. Zhang, C. Benedikt Westphalen and M. Quante, *et al.*, Gemcitabine and nab-paclitaxel combined with afatinib in metastatic pancreatic cancer – Results of a phase 1b clinical trial, *Eur. J. Cancer*, 2024, **201**, 113926.
3 B. L. Musher, E. K. Rowinsky and B. G. Smaglo, *et al.*, LOAd703, an oncolytic virus-based immunostimulatory gene therapy, combined with chemotherapy for unresectable or metastatic pancreatic cancer (LOKON001): results from arm 1 of a non-randomised, single-centre, phase 1/2 study, *Lancet Oncol.*, 2024, **25**, 488–500.
4 J. Li, K. Yu and D. Pang, *et al.*, Adjuvant Capecitabine With Docetaxel and Cyclophosphamide Plus Epirubicin for Triple-Negative Breast Cancer (CBCSG010): An Open-Label, Randomized, Multicenter, Phase III Trial, *J. Clin. Oncol.*, 2020, **38**, 1774–1784.
5 J. F. Lovell, C. S. Jin, E. Huynh, H. Jin, C. Kim, J. L. Rubinstein, W. C. W. Chan, W. Cao, L. V. Wang and G. Zheng, Porphysome nanovesicles generated by porphyrin bilayers for use as multimodal biophotonic contrast agents, *Nat. Mater.*, 2011, **10**, 324–332.
6 H. Bian, D. Ma, X. Zhang, K. Xin, Y. Yang, X. Peng and Y. Xiao, Tailored Engineering of Novel Xanthonium Polymethine Dyes for Synergetic PDT and PTT Triggered by 1064 nm Laser toward Deep-Seated Tumors, *Small*, 2021, **17**, e2100398.
7 L. Cheng, C. Wang, L. Feng, K. Yang and Z. Liu, Functional Nanomaterials for Phototherapies of Cancer, *Chem. Rev.*, 2014, **114**, 10869–10939.
8 Q. Chen, L. Xu, C. Liang, C. Wang, R. Peng and Z. Liu, Photothermal therapy with immune-adjuvant nanoparticles together with checkpoint blockade for effective cancer immunotherapy, *Nat. Commun.*, 2016, **7**, 1–13.

9 G. Alfranca, D. Cui and J. M. de la Fuente, The True Complexity of Photothermal Therapy: A Brief Perspective, *Nano Biomed. Eng.*, 2017, **9**, 129–134.
10 L. Luo, W. Sun, Y. Feng, R. Qin, J. Zhang, D. Ding, T. Shi, X. Liu, X. Chen and H. Chen, Conjugation of a Scintillator Complex and Gold Nanorods for Dual-Modal Image-Guided Photothermal and X-ray-Induced Photodynamic Therapy of Tumors, *ACS Appl. Mater. Interfaces*, 2020, **12**, 12591–12599.
11 C. Wang, W. Zhong, X. Sun, J. Guo, Y. Chen, Y. Zhao, J. Han and Y. Zhao, NIR-Activable Charge Transfer Agents for Synergistic Photoimmunotherapy, *Angew. Chem., Int. Ed.*, 2024, **64**, e202416828.
12 X. Li, J. F. Lovell, J. Yoon and X. Chen, Clinical development and potential of photothermal and photodynamic therapies for cancer, *Nat. Rev. Clin. Oncol.*, 2020, **17**, 657–674.
13 N. Wang, Z. Zhao and X. Xiao, *et al.*, ROS-responsive self-activatable photosensitizing agent for photodynamic-immunotherapy of cancer, *Acta Biomater.*, 2023, **164**, 511–521.
14 X. Wu, H. Yang and X. Chen, *et al.*, Nano-herb medicine and PDT induced synergistic immunotherapy for colon cancer treatment, *Biomaterials*, 2021, **269**, 120654.
15 J. Lee, Y. H. Lee, C. B. Jeong, J. S. Choi, K. S. Chang and M. Yoon, Gold nanorods-conjugated TiO2 nanoclusters for the synergistic combination of phototherapeutic treatments of cancer cells, *J. Nanobiotechnol.*, 2018, **16**, 104.
16 J. Wu, T. Liu, Z. Rios, Q. Mei, X. Lin and S. Cao, Heat Shock Proteins and Cancer, *Trends Pharmacol. Sci.*, 2017, **38**, 226–256.
17 J. Saini and P. K. Sharma, Clinical, Prognostic and Therapeutic Significance of Heat Shock Proteins in Cancer, *Curr. Drug Targets*, 2018, **19**, 1478–1490.
18 L. Guo, H. Peng, R. Shen, J. Ping, F. You, Y. Wang, M. Song and Q. Zhen, Iridium-Based Dual-Functional Nanoparticles for Far-Red Imaging and Photodynamic Therapy, *Nano Biomed. Eng.*, 2017, **9**, 1–8.
19 J. Trepel, M. Mollapour, G. Giaccone and L. Neckers, Targeting the dynamic HSP90 complex in cancer, *Nat. Rev. Cancer*, 2010, **10**, 537–549.
20 G. Chiosis, C. S. Digwal, J. B. Trepel and L. Neckers, Structural and functional complexity of HSP90 in cellular homeostasis and disease, *Nat. Rev. Mol. Cell Biol.*, 2023, **24**, 797–815.
21 J. Feng, W.-X. Ren, F. Kong, C. Zhang and Y.-B. Dong, Nanoscale covalent organic framework for the low-temperature treatment of tumor growth and lung metastasis, *Sci. China Mater.*, 2022, **65**, 1122–1133.
22 X. Tang, C. Chang, M. Hao, M. Chen, D. T. Woodley, A. H. Schönthal and W. Li, Heat shock protein-90alpha (Hsp90α) stabilizes hypoxia-inducible factor-1α (HIF-1α) in support of spermatogenesis and tumorigenesis, *Cancer Gene Ther.*, 2021, **28**, 1058–1070.
23 P. Liu, Y. Peng, Y. Zhou, X. Shi, Q. Li, J. Ding, Y. Gao and W. Zhou, Rapamycin as a ''One-Stone-Three-Birds'' Agent for Cooperatively Enhanced Phototherapies Against Metastatic Breast Cancer, *ACS Appl. Mater. Interfaces*, 2021, **13**, 25674–25684.
24 Y. Okawa, T. Hideshima and P. Steed, *et al.*, SNX-2112, a selective Hsp90 inhibitor, potently inhibits tumor cell growth, angiogenesis, and osteoclastogenesis in multiple myeloma and other hematologic tumors by abrogating signaling via Akt and ERK, *Blood*, 2009, **113**, 846–855.
25 G. N. Masoud and W. Li, HIF-1α pathway: role, regulation and intervention for cancer therapy, *Acta Pharm. Sin. B*, 2015, **5**, 378–389.
26 G. Gao, Y. W. Jiang, W. Sun, Y. Guo, H. R. Jia, X. W. Yu, G. Y. Pan and F. G. Wu, Molecular Targeting-Mediated Mild-Temperature Photothermal Therapy with a Smart Albumin-Based Nanodrug, *Small*, 2019, **15**, 1–15.
27 Y. Zou, D. Huang, S. He, X. Song, W. Liu, W. Sun, J. Du, J. Fan and X. Peng, Cooperatively enhanced photothermal-chemotherapy via simultaneously downregulating HSPs and promoting DNA alkylation in cancer cells, *Chem. Sci.*, 2022, **14**, 1010–1017.
28 M. Park, E. Jung and J. M. Park, *et al.*, The HSP90 inhibitor HVH-2930 exhibits potent efficacy against trastuzumab-resistant HER2-positive breast cancer, *Theranostics*, 2024, **14**, 2442–2463.
29 J. A. Friedman, S. C. Wise and M. Hu, *et al.*, HSP90 inhibitor SNX5422/2112 targets the dysregulated signal and transcription factor network and malignant phenotype of head and neck squamous cell carcinoma, *Transl. Oncol.*, 2013, **6**, 429–441.
30 J. D. Martin, H. Cabral, T. Stylianopoulos and R. K. Jain, Improving cancer immunotherapy using nanomedicines: progress, opportunities and challenges, *Nat. Rev. Clin. Oncol.*, 2020, **17**, 251–266.
31 I. de Lázaro and D. J. Mooney, Obstacles and opportunities in a forward vision for cancer nanomedicine, *Nat. Mater.*, 2021, **20**, 1469–1479.
32 M. R. Laughter, A. L. Nelson, M. Bortot, B. Pena, B. Liu and D. Park, Multifunctional Fluorocarbon-conjugated Nanoparticles of Varied Morphologies to Enhance Diagnostic Effects in Breast Cancer, *Nano Biomed. Eng.*, 2021, **13**, 52–61.
33 T. M. Allen and P. R. Cullis, Drug Delivery Systems: Entering the Mainstream, *Science*, 2004, **303**, 1818–1822.
34 A. M. Scott, J. D. Wolchok and L. J. Old, Antibody therapy of cancer, *Nat. Rev. Cancer*, 2012, **12**, 278–287.
35 Y. Feng, Y. Cheng and Y. Chang, *et al.*, Time-staggered delivery of erlotinib and doxorubicin by gold nanocages with two smart polymers for reprogrammable release and synergistic with photothermal therapy, *Biomaterials*, 2019, **217**, 119327.
36 Z. Luo and J. Jiang, pH-sensitive drug loading/releasing in amphiphilic copolymer PAE–PEG: Integrating molecular dynamics and dissipative particle dynamics simulations, *J. Controlled Release*, 2012, **162**, 185–193.
37 T. Entradas, S. Waldron and M. Volk, The detection sensitivity of commonly used singlet oxygen probes in aqueous environments, *J. Photochem. Photobiol., B*, 2020, **204**, 111787.
38 R. Li, Y. Zhou, Y. Liu, X. Jiang, W. Zeng, Z. Gong, G. Zheng, D. Sun and Z. Dai, Asymmetric, amphiphilic RGD

conjugated phthalocyanine for targeted photodynamic therapy of triple negative breast cancer, *Signal Transduction Targeted Ther.*, 2022, **7**, 64.

39 J. Yan, X. Ma, D. Liang, M. Ran, D. Zheng, X. Chen, S. Zhou, W. Sun, X. Shen and H. Zhang, An autocatalytic multicomponent DNAzyme nanomachine for tumor-specific photothermal therapy sensitization in pancreatic cancer, *Nat. Commun.*, 2023, **14**, 6905.

40 X. Liu, M. Zhang and P. Wang, *et al.*, Nanoscale distribution of bioactive ligands on biomaterials regulates cell mechanosensing through translocation of actin into the nucleus, *Proc. Natl. Acad. Sci. U. S. A.*, 2025, **122**, e2501264122.

41 G. L. Semenza, Hypoxia-inducible factors: mediators of cancer progression and targets for cancer therapy, *Trends Pharmacol. Sci.*, 2012, **33**, 207–214.

42 M. Li, Y. Wang, M. Li, X. Wu, S. Setrerrahmane and H. Xu, Integrins as attractive targets for cancer therapeutics, *Acta Pharm. Sin. B*, 2021, **11**, 2726–2737.

43 H. Chen, H. Song and Y. Luo, *et al.*, Transcytosis Mediated Deep Tumor Penetration for Enhanced Chemotherapy and Immune Activation of Pancreatic Cancer, *Adv. Funct. Mater.*, 2023, **33**, 2214937.

44 H. Song, H. Chen and Q. Chen, *et al.*, Size and Charge Dual-Switchable Nanoparticles for Achieving Chemosensitization and Immune Infiltration against Pancreatic Ductal Adenocarcinoma, *Adv. Funct. Mater.*, 2025, **35**, 2411643.

45 F. Li, W. Si, L. Xia, D. Yin, T. Wei, M. Tao, X. Cui, J. Yang, T. Hong and R. Wei, Positive feedback regulation between glycolysis and histone lactylation drives oncogenesis in pancreatic ductal adenocarcinoma, *Mol. Cancer*, 2024, **23**, 90.

46 X. Feng, Y. Zhang, W. Lin, J. Li, F. Wu, Q. Lu, H. Song, H. Zhang, F. Lan and J. Lu, A Self-Amplifying Photodynamic Biomedicine for Cascade Immune Activation Against Triple-Negative Breast Cancer, *Small*, 2025, **31**, e2410214.

47 B. Wu, Z. Wang and J. Liu, *et al.*, Dual rectification of metabolism abnormality in pancreatic cancer by a programmed nanomedicine, *Nat. Commun.*, 2024, **15**, 10526.

48 F. H. Schopf, M. M. Biebl and J. Buchner, The HSP90 chaperone machinery, *Nat. Rev. Mol. Cell Biol.*, 2017, **18**, 345–360.

49 Y. Miyata, H. Nakamoto and L. Neckers, The Therapeutic Target Hsp90 and Cancer Hallmarks, *Curr. Pharm. Des.*, 2013, **19**, 347–365.

50 J. H. Mo, I. J. Choi, W. J. Jeong, E. H. Jeon and S. H. Ahn, HIF-1α and HSP90: Target molecules selected from a tumorigenic papillary thyroid carcinoma cell line, *Cancer Sci.*, 2012, **103**, 464–471.

51 C. Gola, S. Iussich and S. Noury, *et al.*, Clinical significance and in vitro cellular regulation of hypoxia mimicry on HIF-1α and downstream genes in canine appendicular osteosarcoma, *Vet. J.*, 2020, **264**, 105538.

52 E. Monti, E. Marras, P. Prini and M. B. Gariboldi, Luteolin impairs hypoxia adaptation and progression in human breast and colon cancer cells, *Eur. J. Pharmacol.*, 2020, **881**, 173210.

53 M. Liu, W. Song and L. Huang, Drug delivery systems targeting tumor-associated fibroblasts for cancer immunotherapy, *Cancer Lett.*, 2019, **448**, 31–39.

54 G. Gao, X. Sun, X. Liu, Y. W. Jiang, R. Tang, Y. Guo, F. G. Wu and G. Liang, Intracellular Nanoparticle Formation and Hydroxychloroquine Release for Autophagy-Inhibited Mild-Temperature Photothermal Therapy for Tumors, *Adv. Funct. Mater.*, 2021, **31**, 1–10.

55 R. Xing, Q. Zou, C. Yuan, L. Zhao, R. Chang and X. Yan, Self-Assembling Endogenous Biliverdin as a Versatile Near-Infrared Photothermal Nanoagent for Cancer Theranostics, *Adv. Mater.*, 2019, **31**, e1900822.

56 M. Ashrafizadeh, A. Zarrabi and A. Bigham, *et al.*, (Nano)-platforms in breast cancer therapy: Drug/gene delivery, advanced nanocarriers and immunotherapy, *Med. Res. Rev.*, 2023, **43**, 2115–2176.

57 R. Chang, Q. Zou, L. Zhao, Y. Liu, R. Xing and X. Yan, Amino-Acid-Encoded Supramolecular Photothermal Nanomedicine for Enhanced Cancer Therapy, *Adv. Mater.*, 2022, **34**, e2200139.

58 S. Li, Y. Li, M. Shi, R. Xing, J. C. M. Van Hest and X. Yan, Assembly-enhanced indocyanine green nanoparticles for fluorescence imaging-guided photothermal therapy, *J. Mater. Chem. B*, 2024, **12**, 10915–10922.

